MOX-Report No. 50/2019

A tissue chamber chip for assessing nanoparticle mobility in the extravascular space

Lusi, V.; Moore, T. L.; Laurino, F.; Coclite, A.; Perreira, R.;

Rizzuti, I.; Palomba, R.; Zunino, P.; Duocastella, M.; Mizrahy,

S.; Peer, D.; Decuzzi, P.

A Tissue Chamber Chip for Assessing the Diffusion Propensity of Nanoparticles in the Extravascular Space

Valeria Lusi[1,2], Thomas L. Moore[1], Federica Laurino[1,3], Alessandro Coclite[1], Rui Perreira[1], Ilaria Rizzuti[1], Roberto Palomba[1], Paolo Zunino[3], Marti Duocastella[4], Shoshy Mizrahy[1,5], Dan Peer[5], Paolo Decuzzi*,[1]

1. Laboratory of Nanotechnology for Precision Medicine, Italian Institute of Technology, Via Morego 30, Genoa, 16163, Italy

2. DIBRIS, University of Genova, Via Opera Pia 13, Genoa, 16145, Italy

3. MOX, Department of Mathematics, Politecnico di Milano, Piazza Leonardo da Vinci 32, 20133, Italy

4. Nanophysics, Italian Institute of Technology, Via Morego 30, Genoa, 16163, Italy

5. Laboratory of NanoMedicine, Department of Cell Research and Immunology, Tel-Aviv University, Ramat Aviv, Tel-Aviv, 69978, Israel

* Corresponding author: Dr. Paolo Decuzzi, paolo.decuzzi@iit.it, +39 011 71781 941

Author	ORCID
Thomas L. Moore	0000-0002-7886-5245
Alessandro Coclite	0000-0001-5135-9388
Paolo Zunino	0000-0002-2470-0189
Marti Duocastella	0000-0003-4687-8233
Dan Peer	0000-0001-8238-0673
Paolo Decuzzi	0000-0001-6050-4188

ABSTRACT

Although a plethora of nanoparticle configurations have been proposed over the past 10 years, the uniform and deep penetration of systemically injected nanomedicines into the diseased tissue stays as a major biological barrier. Here, a 'tissue chamber' chip is designed and fabricated to study the extravascular transport of small molecules and nanoparticles. The chamber comprises a collagen slab, deposited within a PDMS mold, and an 800 mm channel for the injection of the working solution. Through fluorescent microscopy, the dynamics of molecules and nanoparticles was estimated within the gel, under different operating conditions. Diffusion coefficients were derived from the analysis of the particle mean square displacements (MSD). For validating the experimental apparatus and the protocol for data analysis, the diffusion D of FITC-Dextran molecules of 4, 40 and 250 kDa was first quantified. As expected, D reduces with the molecular weight of the Dextran molecules. The MSD-derived diffusion coefficients were in good agreement with values derived via fluorescence recovery after photobleaching (FRAP), an alternative technique that solely applies to small molecules. Then, the transport of six nanoparticles with similar hydrodynamic diameters (~ 200 nm) and different surface chemistries was quantified. Surface PEGylation was confirmed to favor the diffusion of nanoparticles within the collagen slab, whereas the surface decoration with hyaluronic acid (HA) chains reduced nanoparticle mobility in a way proportionally to the HA molecular weight. To assess further the generality of the proposed approach, the diffusion of the six nanoparticles was also tested in freshly excited brain tissue slices. In these ex-vivo experiments, the diffusion coefficients were 5-orders of magnitude smaller than for the 'tissue chamber' chip. This was mostly ascribed to the lack of a cellular component in the chip. However, the trends documented for PEGylated and HA-coated nanoparticles in vitro were also confirmed ex-vivo. This work demonstrates that the 'tissue chamber' chip can be employed to effectively and efficiently test the extravascular transport of nanomedicines while minimizing the use of animals.

INTRODUCTION

Since approximately the turn of the millennium, nanoparticles have been promoted as a paradigm-shifting approach to early diagnosis and improved treatment of multiple diseases (Ferrari 2005; Rosenblum et al. 2018). The potential of particle-based drug delivery systems, or in a simple word nanomedicines, to protect drugs (small molecules, biologicals, peptides, etc.) from premature degradation; prolong the circulation time in the blood; reduce systemic toxicity; and control release has been documented extensively by the scientific community (Shi et al. 2017). Moreover, nanomedicines enabled the realization of multifunctional delivery systems with combined therapy and diagnostics (e.g. theranostics) (Nabil et al. 2018; Arranja et al. 2017; Moore et al. 2014), co-delivery of drugs (Blanco et al. 2014; Pushpalatha et al. 2017), and targeted delivery (Tietjen et al. 2018; Lazarovits et al. 2015).

Although several nanomedicines, mostly lipid-based formulations, are under clinical investigation in early and advanced trials, there are still significant challenges in fully integrating nanomedicines into clinical practice. Some of these challenges are merely technical, such as the difficulty in the reproducible synthesis and large-scale manufacturing (Shi et al. 2017), while others are due to challenges in fundamental understanding of particle behavior in complex biological systems (Wilhelm et al. 2016; Hua et al. 2018). To this last point, a major interest in nanomedicine is understanding the transport of particles across biological barriers to their final pathological targets and critical to this goal is understanding the dynamics of particles through the extravascular tissue (Blanco et al. 2015). Researchers have attempted to overcome this grand challenge by tailoring particle physico-chemical properties (i.e. size, surface charge, surface functionalization, material density, shape, etc.), utilizing stimuli-responsive materials, masking particles in cellular coatings, using cells to shuttle particles across barriers, or employing multi-stage delivery systems. For example, Cabral et al. (2011) showed in vivo that particle size (30 to 100 nm) played a significant role in the tumoritropic accumulation of nanoparticles in tumors of varying permeability. That is, size had little effect on particle-tumor accumulation in highly permeable tumors, however when tumors have low permeability the smaller particles (30 nm) accumulate more compared to medium-sized (50 nm) or larger particles (70 and 100 nm). One approach to capitalize on this phenomena is to develop particles that modulate their size throughout their voyage to the target site. Wong, et al. (2011) reported multistage nanoparticles that shrink from approximately 100 nm in diameter to 10 nm as they extravasate from the tumor vasculature into the tumor tissue. This was achieved by having a primary particle which can be actively degraded by proteases in the tumor microenvironment, thereby releasing smaller non-degraded particles (i.e. 10 nm quantum dots). In this case, the larger primary particles enable long circulation half-life and passive tumor targeting, and the release of small particles enables deeper tumor penetration. Another such multistage particle system was reported by Tasciotti et al. (2008), where larger, mesoporous silicon primary microparticles were loaded with quantum dots or single-walled carbon nanotubes (SWCNTs). This system takes advantage of the micron-sized and specifically-shaped primary particles' ability to marginate in the vasculature to better deliver the nano-sized quantum

dots or SWCNTs. Finally, biomimetic approaches are attempting to utilize naturally occurring cellular processes to transport particles across biological barriers. Particles have been coated in "stealth" cellular membranes to avoid immunological detection and clearance, and improve tumor targeting (Hu et al. 2011; Pitchaimani et al. 2019). Moreover, particles have been attached to cells as "hitchhikers" (Anselmo et al. 2015; Brenner et al. 2018) or transported across biological barriers as intracellular cargo (Choi et al. 2012; Moore et al. 2017; Zhang et al. 2018). Despite all of these innovative approaches to optimize particle transport across biological barriers, there exists a need to understand particle transport through tissues on a fundamental level.

In vivo disease models are the benchmark for studying particle transport processes as they are dynamic, complex, and mimic the biological fate of particles in human biology. However, organs-on-chips technologies are increasingly being looked at as alternatives to animal models (Sontheimer-Phelps et al. 2019). These technologies are developed with increasing complexity (i.e. able to mimic organ and organ systems), while providing precise control over the system engineering and parameters. We report here a tissue chamber capable of studying the diffusivity of particles through an extravascular tissue-mimic in real-time. Importantly, we aimed to understand and quantify particle diffusivity both in vitro through the tissue chamber as well as in ex vivo brain tissue. The tissue chamber was realized by fabricating a collagen gel containing a cylindrical tube throughout the center. The transport properties of small-molecule fluorescent dyes (FITC-labelled dextran with varying molecular weights), 200 nm polystyrene beads or spherical PLGA nanoparticles coated with different amounts of poly(ethylene glycol) (PEG), and liposomes coated with different molecular weight hyaluronic acids were determined through fluorescent microscopy. Image analysis was then performed to evaluate the mean square displacement and subsequently the diffusivity of these different agents. These data were then compared to particle diffusion following injection in ex-vivo brain slices.

MATERIALS AND METHODS

Materials. Collagen type I (4 mg/ml) from bovine origin and dextran with different molecular weights 4, 40, and 250 kDa were purchased from Sigma Aldrich (Sigma Aldrich, USA). Dulbecco's Phosphate Buffered Saline (DPBS) was acquired from Gibco Life technologies UK and Fluoresbrite™ carboxy nyo 0.20 μm microspheres were purchased from Polysciences, Inc. (Warrington PA). Poly(lactic-co-glycolic acid) PLGA (50:50, carboxy-terminated, MW 38,000-54,000 Da) was purchased from Sigma Aldrich (St. Louis, MO, USA); 1,2-dipalmitoyl-sn-glycero-3-phosphocholine (DPPC), DSPE-PEG(2000) Carboxylic Acid, DSPE-RhB (Liss Rhod PE), DSPE-EGG, 1,2-Dipalmitoyl-*sn-glycero*-3-phoshoethanolamine (DPPE) and cholesterol (Chol) were obtained from Avanti Polar Lipids (Alabaster, Alabama). Pure soybean phosphatidylcholine (Phospholipon 90G) (PC) was a kind gift from Phospholipid GmbH (Germany).

4

Sodium hyaluronate was purchased from Lifecore Biomedical, LLC (MN,USA). O.C.T. mounting medium compound for cryotomy was purchased from VWR Chemicals. Permount Mounting Media was purchased from Fisher Scientific.

Synthesis of spherical polymeric nanoconstructs (SPNs). Spherical Polymeric Nanoparticles (SPNs) tagged with different amounts of PEG were prepared by a slightly modified sonication-emulsion technique according to previously described procedures (Lee et al. 2016). Two different configurations were prepared to obtain SPNs tagged with 80% or 20% of PEG on the outside surface. On both preparations, 20% of DSPE-RhB was included. Briefly, carboxyl-terminated PLGA and DPPC, in a 10:1 ratio, were dissolved in chloroform to obtain a homogeneous solution (oil phase). For the surface lipid monolayer with 80% PEG, two lipids were used (DSPE-PEG-COOH and DSPE-RhB) with a molar ratio of 5:1, dissolved in aqueous phase (4% ethanol). For the surface lipid monolayer with 20% PEG, three lipids were used (DSPE-PEG-COOH, DSPE-RhB and DSPE-EGG) with a molar ratio of 1:1:3, dissolved in aqueous phase (4% ethanol). The ratio between the oil phase and the aqueous phase was 1 to 5. Afterwards, the oil phase was added drop wisely to the aqueous phase under ultrasonication. The obtained emulsion was then placed under magnetic stirring to facilitate solvent evaporation. SPNs were centrifuged first for 5 minutes at 254 g to settle down any possible debris and then the supernatant was centrifuged 3 more times for 20 minutes at $1,8 \times 10^4$ g.

Preparation of liposomes. Liposomes were synthesized according to previously published procedures (Mizrahy et al. 2014). With minor modifications, Multilamellar Vesicles (MLVs) were made by a mixture of PC, Chol and DPPE in a molar ratio of 60:20:20 (Peer and Margalit 2000; Peer and Margalit 2004; Peer et al. 2008; Kedmi et al. 2010). In brief, lipids were dissolved in ethanol, dried under reduced pressure in a rotary evaporator (Buchi Rotary Evaporator Vacuum System Flavil, Switzerland) and afterwards were hydrated using a PBS solution at pH 7.4. MLVs also contained 0.5% Cy5 labeled DPPE (Mizrahy et al. 2014). At the end, MLVs were vortexed followed by 2h of incubation in a shaker bath at 37 °C. Then, MLVs were extruded by the use of Lipex extrusion device (Northern lipids, Vancouver, Canada) at 65 °C and under 200-500 psi nitrogen pressure. Extrusion was accomplished in several steps using decreasing pore-size polycarbonate membranes (Whatman Inc., UK), performing numerous cycles per pore-size, in order to obtain unilamellar vescicles with a size ranging between 100 and 200 nm in diameter.

Surface modifications of liposomes. The liposome surface modification was made according to previous reported procedures (Landesman-Milo et al. 2013). In brief, high and low molecular weight hyaluronic acid (700 and 5kDa, respectively) (Lifecore Biomedical LL,USA) were dissolved in 0.2 M MES buffer (pH 5.5) to reach a final concentration of 5 mg/ml or 40 mg/ml. Hyaluronic Acid (HA) was activated for 30 minutes with ethyl-dimethyl-aminopropyl-carbodiimide (EDC) (Sigma-Aldrich, USA) and sulfo-NHS (Proteochem) using a molar ratio of 1:1:6

between HA, EDC and sulfo-NHS. Afterwards, liposomes was added and pH was adjusted to 7.4. The solution was then incubated at room temperature for 2 h and the free HA was removed by washing via centrifugation at 4 °C for 60 minutes at 1.3×10^5 g .

Size and stability characterization of nanoparticles. Dynamic light scattering (DLS, Malvern Zetasizer Nano S) was employed to characterize the size and zeta potential of nanoparticles under hydrated conditions at pH 7.0. Nanoparticle stability was performed in water at 37 °C, following the size variation through DLS measurement. The same instrument was used to determine liposomes size and zeta potential for 5 days at 37 °C using HEPES 1M for the size and DI water for the z potential.

Tissue chamber fabrication. Our Tissue Chamber device was fabricated with polydimethylsiloxane (PDMS) using a pre-polymer solution of Sylgard 182 mixed with the curing agent in a 10:1 ratio w/w. This solution was poured in a petri dish to create a 3.5 mm thick PDMS sheet. The petri dish with PDMS was degassed in a vacuum chamber and cured in the oven at 60 °C overnight. After 15 minutes at room temperature the petri was cooled to -20 °C for 1 h before removing the sheet from the base. The PDMS sheets were cut into $15 \times 15 \times 3.5$ mm^3 parallelepipeds, and a $5 \times 5 \times 3.5$ mm^3 empty space for the Tissue Chamber was cut into the center. The PDMS Tissue Chamber was irreversibly bonded to a glass microscope slide (VWR) using oxygen plasma. At the end of the process, a 0.8 mm diameter needle (Sterican B. Braun) was used to generate a channel in the tissue chamber from side to side. At the very end, chips were sterilized by autoclave and dried in incubator overnight. **Figure 1** illustrates the Tissue Chamber fabrication and final geometry.

Collagen type I gel preparation. Collagen type I pH and ionic strength were adjusted by addition of the buffer solution (pH 7.4) to achieve a final pH between 7 and 7.4, with a final concentration of 1.5 mg/ml. 150 µl of collagen type I solution was injected inside the Tissue Chamber and polymerization occurred at 37 °C for 1 h. Next, gels were covered with 50 µl of DPBS to keep them in a hydrated state. After one hour, the needle was removed and the channel was confirmed by optical microscope images (**Figure 1**).

Diffusion assays. Samples were placed under an inverted optical microscope equipped (Leica DMI 6000 B) with a DFC360 FX digital fluorescence camera. Different molecules and particles were injected to study the diffusion through the collagen hydrogel: Dextran 4, 40 and 250 kDa, 200 nm Fluoresbrite® carboxylate microspheres, SPNs and liposomes with different PEG and HA amounts. Fluoresbrite® carboxylate microspheres (from now on called NP200) are commercially available monodispersed fluorescent polystyrene microspheres. These microspheres were provided as a 2.5% aqueous suspensions and injected in the tissue chamber at 0.05% (w/v), SPNs 20% PEG and SPNs 80% PEG

were injected at the same ratio (0.05% w/v). Solutions of Dextran 4, 40 and 250 kDa were injected at 0.5 mg/ml and the 3 different kinds of liposomes were injected at stock concentrations (lipid 40 mg/ml). Images were collected every 30 seconds for 4.5 minutes for the Dextran 4, 40 and 250 kDa (5 μl); every minute for 10 minutes in the case of NP200; every 4 seconds for 44 seconds for all SPNs and liposomes (5 μl).

Mean square displacement (MSD). By tracking the colored wave-front inside the Tissue Chamber collagen over time, the overall diffusion coefficient D was determined as

$$D = \frac{MSD}{2T}$$

(1)

where T is the time interval and the mean square displacement (MSD) were calculated from:

$$MSD = <\Delta x(j\Delta t)^2>$$

(2)

With the j index running on the total number of Δt in T and x represents the height of colored channel at time t (Valentine et al. 2004) .The heights of the channel at different time point are obtained offline by post processing the fluorescence images using ImageJ. For the results presented in this paper, the MSD was plotted over time and the diffusion coefficient was determined as half of the slope of the curve fitting the experimental points.

Fluorescence recovery after photobleaching (FRAP). In this analysis, experiments were conducted using a confocal laser scanning microscope (CLSM) Nikon Confocal microscope A1R with a plan apo DIC N2 20X/ 0.75 objective. A 488 nm Argon ions laser line was used to excite the samples and a bandpass 500-550 filter was placed before the photomultiplier tube. The collagen solution was placed in μ-Dish Micro-Insert 4 well (Ibidi, Germany) and 10 μl of neutralized collagen type I was polymerized at 37 °C for 1 h. Each tissue chamber was injected with 23 nl using a nanoinjector (Drummond "Nanoject II" automatic nanoliter injector), following manufacturer's instructions. Injection velocity was 23 nl/s. The Nanoject II required pulled micropipets with a capillary outer diameter of 1140 μm and inner diameter of 530 μm. Experiments were performed at equilibrium, generally 12-48 hours post injection depending on the MW of the molecule. Using a circular region of interest (ROI) with a radius of 92.5 μm, gels were first bleached with a laser for 20 minutes and then the recovery of fluorescence was observed in the following 20 minutes. The recovery of fluorescence in the bleached ROIs gave the diffusion coefficient. The software provides the curve associated with bleaching and recovery as well as the parameter τ_D, which is related to the diffusion coefficient through the following formula:

$$\tau_D = \frac{\omega^2}{4D}$$

(3)

where ω is the radius of the ROI and D is the diffusion coefficient (Erikson et al. 2008).

Quantification of the diffusion coefficient via error minimization algorithm (EMA). This technique is useful when FRAP and MSD cannot be applied. It is rather general and robust as it takes as an input the raw data from the diffusion assays (**Figure 6**). An efficient algorithm for fitting a vector of parameters on a given dataset is developed (Tröltzsch 2010). The parameters are interpreted as control variables in an optimization problem that minimizes a functional representing the difference between the experimental observations and the model predictions. The collagen gel in the Tissue Chamber chip is described as a rectangular domain Ω in which, at the initial time, a concentration $c(x,y,0) = c_{inj}(x,y)$ of molecules is prescribed. The temporal evolution of the concentration $c = c(x,y,t)$ in the time interval $[0,T]$ is described by:

$$\begin{cases} \frac{\partial c}{\partial t} - D\Delta c = 0 & \text{in } \Omega, t > 0, \\ D\nabla c \cdot \boldsymbol{n} = 0 & \text{on } \partial\Omega \times (0,T), \\ c = c_{inj} & \text{in } \Omega, t = 0, \end{cases} \tag{4}$$

where $\Delta u = \partial_{xx} u + \partial_{yy} u$ is the Laplace operator and $c_{inj} = c_{inj}(x,y)$ is an assigned function obtained processing the fluorescence images at time $t = 0$ using the algorithm summarized in steps 1, 2, 3, 4 described in what follows. The system can be readily solved numerically if D is known (direct problem). For the inverse problem, D is not known a priori. In this case, the solution is obtained by minimizing the following functional J:

$$\min J(D) = \frac{1}{2}||c(T) - \bar{c}(T)||^2_{L^2(\Omega)} + \frac{\lambda}{2}|D|^2, \tag{5}$$

subject to the eq.(4). The first term in J gives the difference between the experimentally observed concentration field $\bar{c}$ at T and the concentration field c, which is computed at time T using eq.(4) under a specific assumption for D. The second term $\frac{\lambda}{2}|D|^2$ is a regularization operator. For the Lagrangian principle, the optimal diffusion parameter is the solution of the unconstrained minimization problem $\min \mathcal{L}(c,D,p)$ where $\mathcal{L}$ is the Lagrangian functional, defined as follows

$$\mathcal{L}(c,D,p) = J(c,D) - \int_0^T \int_\Omega \frac{\partial c}{\partial t} p - \int_0^T \int_\Omega D\nabla c \cdot \nabla p \tag{6}$$

where p is the so called Lagrange multiplier. For the space discretization, an admissible triangulation of the domain Ω is introduced and the linear finite element method is applied (**<u>Figure 6</u>**). For time discretization, the backward Euler scheme is chosen. To evaluate the functional J, the finite element approximation of the state equations must be compared with the observed concentration field $\bar{c}$. To this end, the pixel map of $\bar{c}$ is converted into a finite element function. This is achieved by means of image analysis tools as per the following protocol: 1. conversion of the RGB picture for $\bar{c}$ into a gray scale image; 2. generation of a mesh with triangular elements having the same dimensions as

pixel number of the image; 3. definition of a finite element variable that accounts for the grey level for each pixel; 4. projection of the previous gray scale map on a coarse mesh of triangular elements used for the solution of the finite element method applied to eq.(4). The minimization of the Lagrangian functional is achieved by means of a Non Linear Conjugate Gradient iterative method, which, given a starting value for D, solves eq.(4), then computes the functional *J*, solves for the adjoint equation to estimate *p*, and evaluates the derivative of $\mathcal{L}$ with respect to D. If this is sufficiently close to zero then the correct value for D is returned. If this is not close to zero, then it updates the diffusion coefficient estimation and it runs again the full analysis starting a new iteration.

E*x-vivo* experiments. Wild-type C57BL/6 mice aged 2-6 months were sacrificed to obtain 2.0 mm brain tissue slices via a Zivic Mouse brain slicer. The striatum of these tissues was injected with 69 nl of a solution containing approximately 1,000 nanoparticles for each experiment using the nanoinjector with a velocity of 23 nl/s. Injected slices were placed in a custom-made three-dimensional (3D) particle tracking system consisting of a wide-field inverted microscope (Nikon Ti) with an oil-immersion objective (Nikon 100x Plan Apo VC 100x/1.4 oil DIC N2), a piezoelectric stage (Mad City Lab) and a single EMCCD camera (DU897DCS-BV Andor Technology) (Sancataldo et al. 2017; Zhang et al. 2017). Sequential images of multiple nanoparticles were recorded at 10 frames per second (fps) in time slots of 40 s (Zhang et al. 2017). At the end, the 3D particle trajectories and the corresponding Mean Square Displacement were calculated by post processing the movies with Fiji and a custom Matlab script (Schindelin et al. 2012).

RESULTS

The Tissue Chamber apparatus for the diffusion experiments. The Tissue Chamber chip consists of a polydimethylsiloxane (PDMS) rectangular slab ($15 \times 15 \times 3.5$ mm) in which an empty space of $5 \times 5 \times 3.5$ mm is realized by direct cutting. The resulting chamber is bonded to a microscopy glass slide via oxygen plasma treatment (**Figure 1A**). Next, a 0.8 mm needle is placed at half the height of the PDMS walls, crossing the length of the empty space. The empty space is then filled with a collagen solution which is incubated at 37 °C, thereby allowing the collagen to gel around the needle. The needle is then removed, which leaves behind a channel within the collagen matrix. **Figure 1A** shows side and top schematic views of the tissue chamber. These images highlight the geometry of the chip and the confinement of the collagen (represented as a pink solution) within the chamber. The chip is realized to study the diffusion of molecules and nanoparticles into the extravascular tissue upon injection into the channel via fluorescent microscopy. **Figure 1B** shows the different steps in the analysis, which includes the chip realization; the injection of the test solution (e.g. dextran-dye or particles) via a pipette NanoInjector or syringe pump; the microscopy

acquisition, and image post-processing and mathematical analysis. Specifically, in order to perform the diffusion measurements, the Tissue Chamber is placed on the stage of an inverted optical microscope (Leica DMI 6000 B) equipped with a DFC360 FX digital fluorescence camera. Fixed volumes of the working solutions are injected in the Tissue Chamber using a NanoInjector. Images are post-processed using ImageJ (https://imagej.nih.gov/) and other custom scripts to estimate the mean square displacement (MSD) and, eventually, the diffusion coefficient of the different molecules and nanoparticles.

Analysis of the diffusion of small molecules within the Tissue Chamber chip. In order to test the chip and the whole measurement apparatus, dextran molecules of different molecular weights were used. Specifically, 5 μl of an aqueous solution containing 4, 40 or 250 kDa FITC-dextran molecules were injected into the Tissue Chamber. The progressive spreading of the green fluorescent solution within the gel is recorded over time. The three top rows of **Figures 2A-C** present the diffusing front of the dextran solutions at different time points, namely 0, 90 and 240 sec. At each time point, the size of the colored area is estimated by post-processing the fluorescent images via the ImageJ software. Note that the size of the channel is about 800 μm, which corresponds to the outer diameter of the needle used for realizing the channel itself within the collagen matrix. The lowest row in **Figures 2A-C** shows the variation over time of the averaged MSD, calculated from the experimental data using eq. (2) in the Methods section. Each point on these plots corresponds to the MSD at that time t, averaged over multiple experiments (n ≥ 5). The slope of the MSD (t) curves provides, through eq. (1), the actual diffusion coefficient. **Figure 2D** summarizes the experimental results providing the diffusion coefficient of the three tested molecules (4, 40 and 250 FITX-dextran) as derived from the MSD measurements in the Tissue Chamber chip (blue bars). As expected, the diffusion coefficient reduces as the molecular weight of dextran increases. For the 4 kDa dextran, a coefficient of diffusion D = 44.20 ± 6.65 μm^2/s is derived. This number reduces by about 28% (D = 32.00 ± 13.51 μm^2/s), for 40 kDa dextran and by about 78% (D = 9.9 ± 3.71 μm^2/s) for 250 kDa dextran.

The Einstein-Stoke relation was used to estimate the diffusion coefficients of the dextran molecules in pure water:

$$D_w = k_B T/(6\pi\mu R_H) \qquad\qquad (7)$$

from which it results that D$_w$ ~270 μm^2/s for 4 kDa dextran, ~40 μm^2/s for 40 kDa dextran, and ~20 μm^2/s for 250 kDa dextran. Indeed, as expected, the diffusion coefficient in water is significantly higher than in the collagen matrix for all dextran molecular weights. However, interestingly, it is the dextran with the smaller molecular weight (4 kDa) that is subjected to the largest reduction (6-fold) in diffusion from ~270 to ~45 μm^2/s. In eq. (7), $k_B T$ is the Boltzmann energy at room temperature (4.11×10^{-21} J), μ is the dynamic viscosity of water (10^{-3} Pa·s), and R_H is the hydrodynamic radius of

the molecule (R_H ~0.8 nm for 4 kDa dextran, ~5 nm for 40 kDa dextran, and ~11.5 nm for 250 kDa dextran (Armstrong et al. 2004). To validate the experimental set-up, the diffusion of dextran molecules in collagen was also assessed via fluorescence recovery after photobleaching (FRAP) returning values in good agreement with those quantified within the Tissue Chamber chip. Specifically, the diffusion coefficients estimated via FRAP were equal to D_{FRAP} = 37.30 ± 5.06 μm^2/s for 4 kDa dextran, 15.20 ± 3.14 μm^2/s for 40 kDa dextran, and 10.10 ± 2.06 μm^2/s for 250 kDa dextran. Only for 40 kDa dextran, there was a statistically significant difference between FRAP and Tissue Chamber measured diffusion coefficients. For all other tested cases the results deriving from the two different techniques are in good agreement. Finally, the diffusion coefficient was also estimated via the EMA approach and compared with the MSD and FRAP results. The EMA was applied using a regularization parameter $\lambda = 10^{-2}$ and, for each experiment. The diffusion coefficient was computed as the average of the diffusion coefficients resulting from the analysis of different time intervals. In particular, D_{EMA} = 81.15 ± 63.09 μm^2/s for 4 kDa Dextran, 49.15 ± 19.73 μm^2/s for 40 kDa Dextran and 13.54 ± 5.38 μm^2/s for 250 kDa Dextran. Interestingly, the higher is the Dextran molecular weight, the smaller is the difference between the results obtained using the EMA and MSD.

Analysis of the diffusion of nanoparticles within the Tissue Chamber chip. In this section, the diffusion of three different nanoparticles within the collagen matrix of the Tissue Chamber chip was studied systematically. In **Figure 3**, schematic representations (first row); scanning electron microscopy images (second row); and the temporal variation of size and surface ζ potential (third row) are presented for the three different nanoparticles: NP 200 – commercially available 200 nm polystyrene nanoparticles; SPN – spherical polymeric nanoparticles with all hydrodynamic diameter of approximately 200 nm; and HA-Lip – liposomes coated with a hyaluronic acid layer returning a hydrodynamic diameter around 200 nm.

The NP 200 nanoparticles have a carboxylated surface, a hydrodynamic diameter of 187.96 ± 2.42 nm and a ζ potential of -42.5 ± 2.12 mV. The stability of these particles was clearly demonstrated by the DLS data documenting a fairly constant hydrodynamic diameter over 5 days of observation (**Figure 3A**, third row). The ζ potential consistently stayed between -40 and -50 mV contributing to the electrostatic repulsion and therefore the colloidal stability of the NP 200. The electron microscopy images of **Figure 3A** (second row) confirm the uniform spherical shape of these particles. The spherical polymeric nanoparticles (SPNs) were synthesized via an emulsion technique and possess a poly(lactic-co-glycolic acid) (PLGA) core stabilized by a lipid monolayer, with polyethylene glycol (PEG) chains (Lee et al. 2016; Stigliano et al. 2015). **Figure 3B** (first row) shows a schematic representation of SPNs documenting the polymeric/lipid structure. Chains of lipid-RhB are included in the surface monolayer thus introducing a fluorescent reporting molecules in the nanoparticle structure. Two different configurations of SPNs are realized depending on the initial PEG content.

For 20% SPN, the initial concentration of lipid-PEG is 20% of the total lipid mass while, for 80% SPN, the initial concentration of lipid-PEG is 80% of the total lipid mass. In both cases, the electron microscopy analysis confirms the spherical shape and monodisperse size distribution of the nanoparticles (**Figure 3B**, second row). At time zero, the DLS returns a hydrodynamic size of 186 ± 13 nm and a ζ potential of -45.9 ± 0.79 mV for the 20% SPNs. The 80% SPNs are slightly smaller with a hydrodynamic size of 170 ± 3 nm and a ζ potential of –39.1 ± 0.87 mV. Indeed, the higher percent of lipid-PEG on the surface fosters particle stabilization, thus reducing the overall hydrodynamic diameter, and further reduces the negative surface electrostatic charge, which is driven by the -COOH groups of the lipid-PEG chains (**Figure 3C**, third row). Note incidentally that these two features demonstrate indirectly that 80% SPNs have a higher lipid-PEG content on their surface as compared to 20% SPNs. The spherical polymeric nanoconstructs are stable over the period of 5 days with an overall variation in hydrodynamic size limited to 10% for both 20% and 80% SPNs (**Figure 3C**, third row). Finally, the third type of nanoparticles schematically presented in the first row of **Figure 3C** are the liposomes with an aqueous core and a lipid bilayer, which is externally coated at different degrees with hyaluronic acid (HA) (Mizrahy et al. 2014). Three different configurations of this HA-Lip are considered: liposomes not coated with any HA layer (uHA-Lip); liposomes coated with a 5kDa HA layer (5HA-Lip); and liposomes coated with a 700 kDa HA layer (700HA-Lip). For the uHA-Lip, the initial hydrodynamic diameter was 146.1± 4.271 nm. This decreases to 138.5 ± 4.845 and 132.4 ± 6.493 nm for the 5HA-Lip and 700Ha-Lip, respectively. The ζ potential is stable at -37 ± 4 mV for all three configurations. SEM and TEM images confirm the DLS data. Specifically, the electron microscopy images in **Figure 3C** (second row) are for the 5HA-Lip (SEM) and for uHA-Lip (TEM). Furthermore, these nanoparticles present good colloidal stability over a 5-days period **Figure 3C** (third row).

After confirming the size and stability of the nanoparticles, diffusion experiments were conducted in the Tissue Chamber chip. Specifically, a 5 μl solution with SPNs or HA-Lip was introduced into the chip and the progressive diffusion within the collagen matrix was recorded over time. The bar charts in **Figure 4A** provides the diffusion coefficients in the collagen matrix for NP 200, the two SPN configurations, and the three HA-Lip configurations. Representative images of NP 200 in the chip, in both brightfield and fluorescence, are given in **Figure 4B**. It is shown that the diffusion coefficient increases from 1.75 ± 0.65 μm^2/s for the NP 200, un-PEGylated nanoparticles to 3.38 ± 1.89 μm^2/s for the 20% SPNs and 4.89 ± 0.25 μm^2/s for the 80% SPNs, which are characterized by the highest surface density of PEG. For the liposomes, the presence of HA over the surface reduces the diffusion coefficient from 5.01 ± 1.96 μm^2/s for the uHA-Lip; to 3.83 ± 1.80 μm^2/s for the 5HA-Lip and 2.21 ± 1.30 μm^2/s for the 700HA-Lip. The theoretical diffusion coefficient through the equation of Einstein-Stokes was also calculated. The diffusion coefficients for the NP 200, 20% SPNs 20% PEG and SPNs 80% PEG using the EMA approach were also computed. In particular, D_{EMA}= 1.75 ± 0.65 μm^2/s for the NP 200, 21.40 ± 7.41 μm^2/s for the SPNs 20% PEG and 6.68 ± 2.56 μm^2/s for the

SPNs 80% PEG. While the D_{EMA} values for NP 200 and 80% SPNs are in good agreement with the MSD-derived diffusion coefficients, EMA fails in predicting accurately the diffusion for the SPNs 20% PEG.

These results emphasize that an increase in PEGylation can more efficiently lubricate the particle-tissue interface and favor the diffusion and tissue penetration (Dancy et al. 2016). For the second group of nanoparticles studied, i.e. liposomes, the diffusion coefficient within the type I collagen gel calculated with the MSD shows that the uHA-Lip diffuse more than the HA coated liposomes, ostensibly due to the interaction of collagen with hyaluronic acid (Annabi et al. 2004). Moreover, the 5HA-Lip diffuse more than 700HA-Lip due to for their greater lubricating effect (Mizrahy et al. 2011).

Analysis of the diffusion of nanoparticles within brain tissue slices. The diffusion of nanoparticles was also assessed in 2 mm thick, freshly excised brain slices from C57BL/6 wild-type mice. A 69 nl of a solution containing the different types of nanoparticles was introduced in the striatum of the brain slices (**Figure 5A-C**). The Nanoinjector was placed at 1.5 mm from the top of the slice and the desired volume was introduced at 0.5 mm from the bottom of the slice (Zhang et al. 2017). The dynamics of the nanoparticles was monitored over time using an inverted microscope specifically modified for single particle tracking, using an oil immersion 100X objective. Representative images are provided in **Figure 5C**. The resulting movies were post-processed through the Fiji trackmate tool (Tinevez et al. 2017) and analyzed with a custom Matlab script, which was specially developed to extrapolate the MSD (Sancataldo et al. 2017). From this analysis, the 2D (x,y) and 3D (x,y,z) trajectories of the individual particles over time can be extracted, as shown in **Figure 5D**. Finally, the mean square displacement of the nanoparticles can be computed and, consequently, the diffusion coefficient is derived as described in the previous paragraphs. The diffusion coefficient for the six different particles are provided by the bar chart in **Figure 5E**. Notably, the trends are similar to the one derived for the same particle in vitro within the collagen matrix of the Tissue Chamber chip. In other words, the diffusion coefficient increase moving from un-PEGylated nanoparticles (NP 200) to PEGylated SPNs, and reduces with the presence of HA on liposomes. Specifically, the diffusion was $2.68 \pm 1.33 \times 10^{-5}$ $\mu m^2/s$ for the NP 200; $4.84 \pm 2.41 \times 10^{-5}$ $\mu m^2/s$ for the 20% SPNs; $5.36 \pm 2.49 \times 10^{-5}$ $\mu m^2/s$ for the 80% SPNs; $6.32 \pm 2.81 \times 10^{-5}$ $\mu m^2/s$ for the uHA-Lip; $3.50 \pm 1.91 \times 10^{-5}$ $\mu m^2/s$ for the 5HA-Lip; and $2.48 \pm 1.35 \times 10^{-5}$ $\mu m^2/s$ for the 700HA-Lip.

Comparing these results with the one obtained in the Tissue Chamber chip, a decrease in the diffusion coefficient of five orders of magnitude is noticed. This is indeed expected given that the Tissue Chamber chip does not include cells in its current configuration.

DISCUSSIONS AND CONCLUSIONS

The fundamental understanding of particle dynamics within complex, 3D matrices (e.g. through extravascular space) is critical to the advancement of nanomedicines into the clinic. A 'Tissue Chamber' chip has been demonstrated for evaluating the mobility of nanoparticles under different biophysical conditions. Specifically, the diffusion of six different nanoparticles (~ 200 nm) was assessed into a collagen gel, mimicking the extravascular matrix of a biological tissue. The coating of spherical, solid polymeric nanoparticles with PEG (2,000 kDa) increased the extravascular mobility as compared to bare nanoparticles. This was mostly ascribed to steric, repulsive forces originating at the PEG interface. On the contrary, surface decoration with HA was responsible for a significant reduction in extravascular mobility, especially at high molecular weights (700 kDa). This was associated with the possible entanglement of long HA chains with the collagen matrix. The proposed Tissue Chamber chip represents a versatile platform supporting fundamental studies on particle diffusion in a tissue-like environment where multiple biophysical parameters can be accurately controlled (e.g. tissue components and porosity). This will allow us to optimize the geometrical and surface properties of nanoparticles to achieve high and uniform tissue penetration.

REFERENCES

B. Annabi, S. Thibeault, R. Moumdjian, R. Béliveau, J. Biol. Chem. **279**, 21888 (2004)

A.C. Anselmo, J.B. Gilbert, S. Kumar, V. Gupta, R.E. Cohen, M.F. Rubner, S. Mitragotri, J. Controlled Release **199**, 29 (2015)

A.G. Arranja, V. Pathak, T. Lammers, Y. Shi, Pharmacol. Research **115**, 87 (2017)

J. K. Armstrong, R.B. Wenby, H.J. Meiselman, T.C. Fisher, Biophys. J **87**, 4259 (2004)

H. Cabral, Y. Matsumoto, K. Mizuno, Q. Chen, M. Murakami, M. Kimura, Y. Tereda, M.R. Kano, K. Miyazono, M. Uesaka, N. Nishiyama, K: Kataoka, Nat. Nanotechnol. **6**, 815 (2011)

E. Blanco, T. Sangai, S. Wu, A. Hsiao, G.U. Ruiz-Esparza, C.A. Gonzalez-Delgado, F.E. Cara, S. Granados-Principal, K.W. Evans, A. Akcakanat, Y. Wang, K.A. Do, F. Meric-Bernstam, M. Ferrari, Mol. Therapy **22** 1310 (2014)

E. Blanco, H. Shen, M. Ferrari, Nat. Biotechnol. **33**, 941 (2015)

J.S. Brenner, D.C. Pan, J.W. Myerson, O.A. Marcos-Contreras, C.H. Villa, P. Patel, H. Hekierski, S. Chatterjee, J.-Q. Tao, H. Parhiz, K. Bhamidipati, T.G. Uhler, E.D. Hood, R.Y. Kiseleva, V.S. Shuvaev, T. Shuvaeva, M. Khoshnejad, I. Johnston, J.V. Gregory, J. Lahann, T. Wang, E. Cantu, W.M. Armstead, S. Mitragotri, V. Muzykantov, Nat. Comm. **9**, 2684 (2018)

M.-R. Choi, R. Bardhan, K.J. Stanton-Maxey, S. Badve, H. Nakshatri, K.M. Stantz, N. Cao, N.J. Halas, S.E. Clare, Cancer Nanotechnol. **3**, 47 (2012)

J.G. Dancy, A.S. Wadajkar, C.S. Schneider, J.R.H. Mauban, O.G. Goloubeva, G.F. Woodworth, J.A. Winkles, A.J. Kim, J. Controlled Release **238**, 139 (2016)

A. Erikson, H.N: Andersen, S.N. Naess, P. Sikorski, C.d.L. Davies, Biopolymers **89**, 135 (2008)

M. Ferrari, Nat. Rev. Cancer **5**, 161 (2005)

C.-M.J. Hu, L. Zhang, S. Aryal, C. Cheung, R.H. Fang, L. Zhang, Proc. Natl. Acad. Sci. **108**, 10980 (2011)

S. Hua, M.B.C. de Matos, J.M. Metselaar, G. Storm, Frontiers Pharmacol. **9**, 790 (2018)

D. Landesman-Milo, M. Goldsmith, S. Leviatan-Ben-Arye, B. Witenberg, E. Brown, S. Leibovitch, S. Azriel, S. Tabak, V. Morad, D. Peer, Cancer Lett. **334**, 221 (2013)

J. Lazarovits, Y.Y. Chen, E.A. Sykes, W.C.W. Chan, Chem. Comm. **51**, 2756 (2015)

A. Lee, D. di Mascolo, M. Francardi, F. Piccardi, T. Bandiera, P. Decuzzi, Nanomed.: Nanotechnol. Biol. Med. **12**, 2139 (2016)

R. Kedmi, N. Ben-Arie, D. Peer, Biomaterials **31**, 6867 (2010)

S. Mizrahy, M. Goldsmith, S. Leviatan-Ben-Arye, E. Kisin-Finfer, O. Redy, S. Srinivasan, D. Shabat, B. Godin, D. Peer, Nanoscale **6**, 3742 (2014)

S. Mizrahy, S.R. Raz, M. Hasgaard, H. Liu, N. Soffer-Tsur, K. Cohen, R. Dvash, D. Landsman-Milo, M.G.E.G. Bremer, S.M. Moghimi, D. Peer, J. Controlled Release **156**, 231 (2011)

T.L. Moore, H. Chen, R. Morrison, F. Wang, J.N. Anker, F. Alexis, Mol. Pharm **11**, 24 (2014)

T.L. Moore, D. Hauser, T. Gruber, B. Rothen-Rutishauser, M. Lattuada, A. Petri-Fink, R. Lyck, ACS Appl. Mater. Interfaces **9**, 18501 (2017)

G. Nabil, K. Bhise, S. Sau, M. Atef, H.A. El-Banna, A. Iyer, Drug Discovery Today, (2018) https://doi.org/10.1016/j.drudis.2018.08.009

D. Peer and R. Margalit, Archives Biochem. Biophysics **383**, 185 (2000)

D. Peer and R. Margalit, Internatl. J. Cancer **108**, 780 (2004)

D. Peer, E.J. Park, Y. Morishita, C.V. Carman, M. Shimaoka, Science **319**, 627 (2008)

A. Pitchaimani, T.D.T. Nguyen, R. Marasini, A. Eliyapura, T. Azizi, M. Jaberi-Douraki, S. Aryal, Adv. Funct. Mater. **29**, 1806817 (2019)

R. Pushpalatha, S. Selvamuthukumar, and D. Kilimozhi, J. Drug Delivery Sci. Technol. **39** 362 (2017)

D. Rosenblum, N. Joshi, W. Tao, J.M. Karp, D. Peer, Nat. Comm. **9**, 1410 (2018)

J. Shi, P.W. Kantoff, R. Wooster, O.C. Farokhzad, Nat. Rev. Cancer **17**, 20 (2017)

E. Tasciotti, X. Liu, R. Bhavane, K. Plant, A.D. Leonard, B.K. Price, M.M.-C. Cheng, P. Decuzzi, J.M. Tour, F. Robertson, M. Ferrari, Nat. Nanotechnol. **3**, 151 (2008)

G.T. Tietjen, L.G. Bracaglia, W.M. Saltzman, J.S. Pober, Trends Mol. Med. **24**, 598 (2018).

J.-Y. Tinevez, N. Perry, J. Schindelin, G.M. Hoopes, G.D. Reynolds, E. Laplantine, S.Y. Bednarek, S.L. Shorte, K.W. Eliceiri, Methods **115**, 80 (2017)

F. Tröltzsch, Optimal Control of Partial Differential Equations, vol. 112 (Graduate studies in mathematics, 2010)

G. Sancataldo, L. Scipioni, T. Ravasenga, L. Lanzanò, A. Diaspro, A. Barberis, M. Duocastella, Optica **4**, 367 (2017)

J. Schindelin, I. Arganda-Carreras, E. Frise, V. Kaynig, M. Longair, T. Pietzsch, S. Preibisch, C. Rueden, S. Saalfeld, B. Schmid, J.Y. Tinevez, D.J. White, V. Hartenstein, K. Eliceiri, P. Tomancak, A. Cardona, Nat. Methods **9**, 676 (2012)

A. Sontheimer-Phelps, B.A. Hassell, D.E. Ingber, Nat. Rev. Cancer, **19**, 65 (2019)

C. Stigliano, J. Key, M. Ramirez, S. Aryal, P. Decuzzi, Adv. Funct. Mater. **25**, 3371 (2015)

M.T. Valentine, Z.E: Perlman, M.L. Gardel, J.H. Shin, P. Matsudaira, T.J. Mitchison, D.A. Weitz, Biophysical J **86**, 4004 (2004)

S. Wilhelm, A.J. Tavares, Q. Dai, S. Ohta, J. Audet, H.F. Dvorak, W.C.W. Chan, Nat. Rev. Mater. **1**, 16014 (2016)

C. Wong, T. Stylianopoulos, J. Cui, J. Martin, V.P. Chauhan, W. Jiang, Z. Popović, R.K. Jain, M.G. Bawendi, D. Fukumura, Proc. Natl. Acad. Sci. **108**, 2426 (2011)

W. Zhang, M. Wang, W. Tang, R. Wen, S. Zhou, C. Lee, H. Wang, W. Jiang, I.M. Delahunty, Z. Zhen, H. Chen, M. Chapman, Z. Wu, E.W. Howerth, H. Cai, Z. Li, J. Xie, Adv. Mater. **30**, 1805557 (2018)

C. Zhang, E.A. Nance, P. Mastorakos, J. Chisholm, S. Berry, C. Eberhart, B. Tyler, H. Brem, J.S. Suk, J. Hanes, J. Controlled Release **263**, 112 (2017)
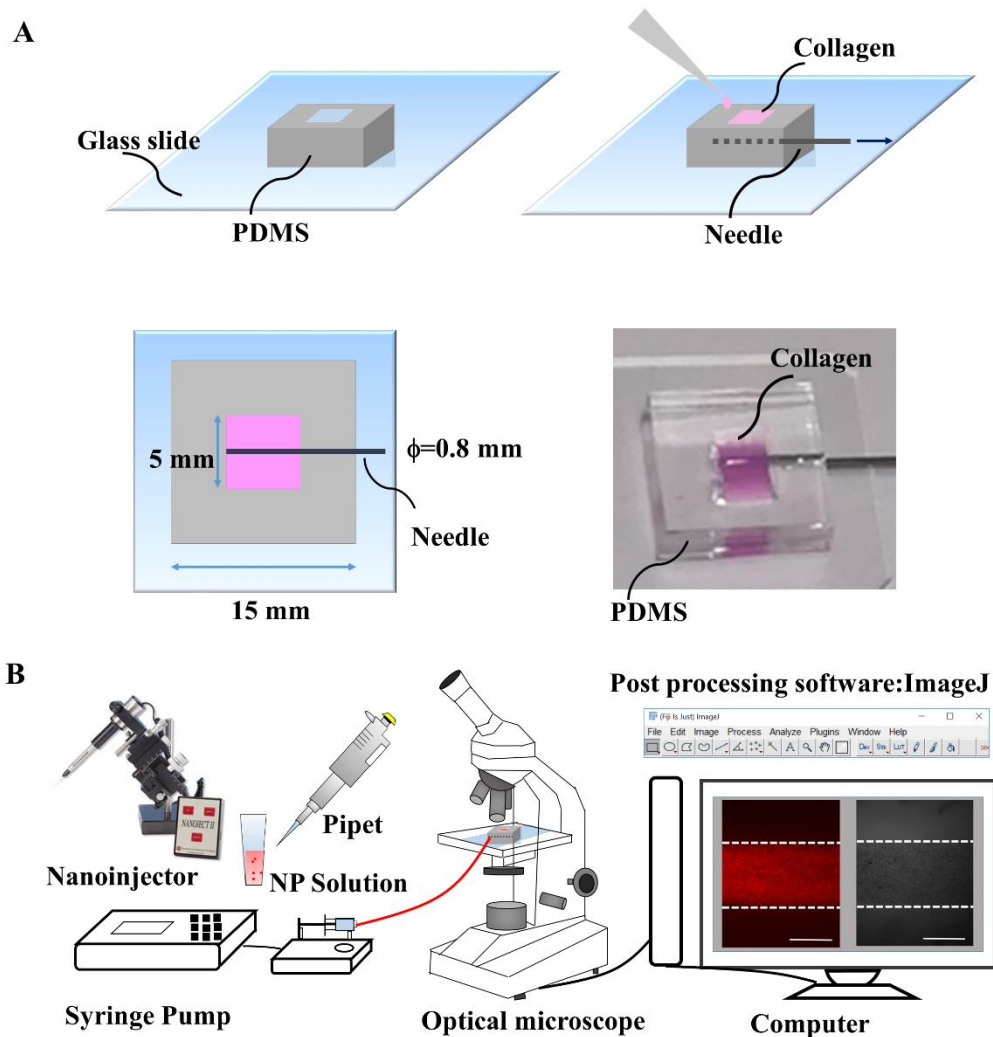
Figure 1. Tissue Chamber microfluidic chip. (A) 3D schematic representation of the Tissue Chamber PDMS chip with a description of channel fabrication process, an overhead view of the Tissue Chamber showing the dimensions, and a photographic image of the tissue chamber bonded on a glass slide and filled with collagen type I. The photograph shows the needle inserted across the chamber which is used to create the channel for injecting tracers. (B) Schematic of the entire experimental setup with representative optical microscopy images of 200 nm beads injected inside the channel: brightfiled (left) and fluorescent (right) images of a channel portion. Scale bars are 500 microns.
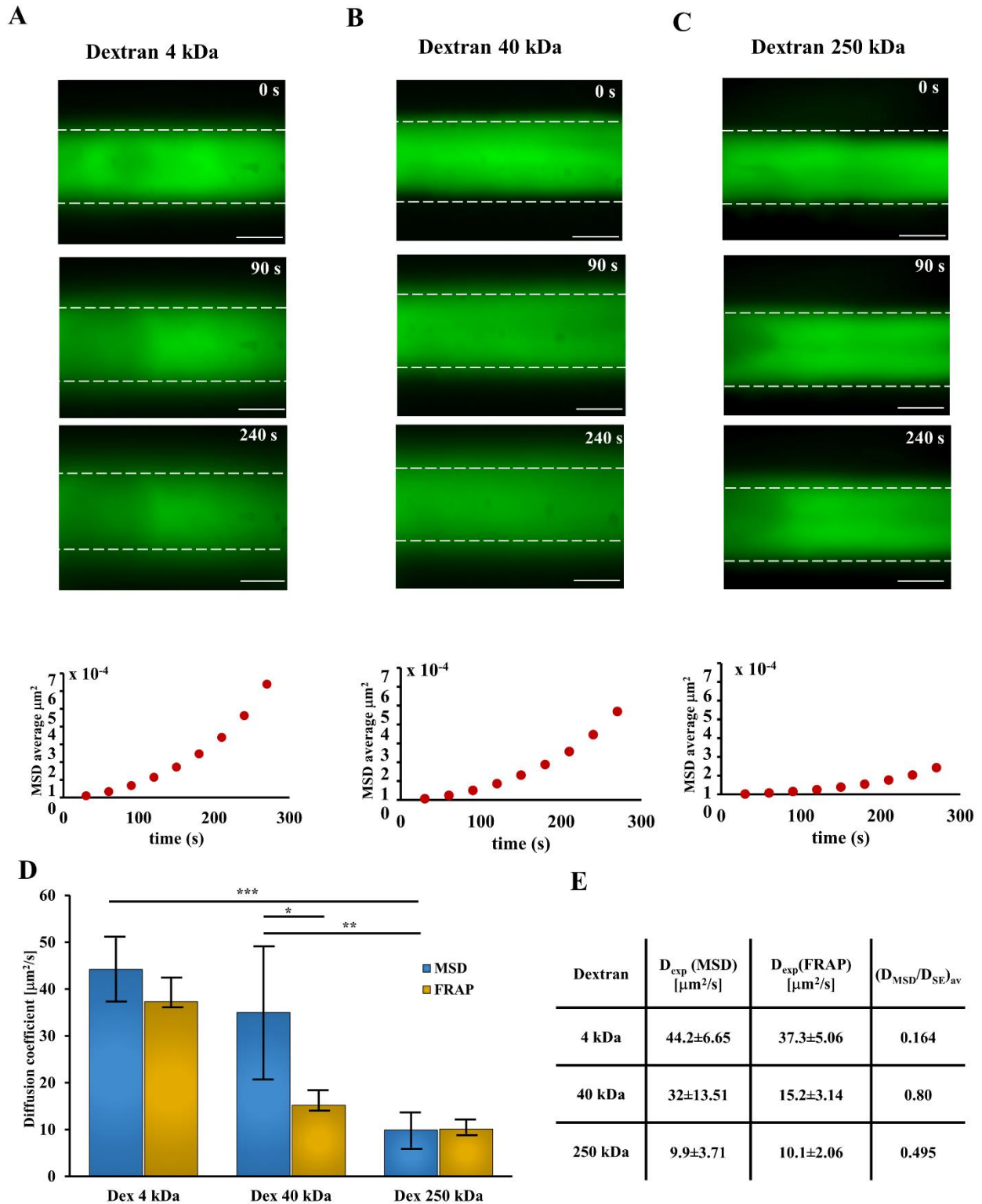
Figure 2. Optical fluorescent microscopy images and quantification of different molecular weight dextran diffusion. Fluorescent images of the channel in the Tissue Chamber filled with (A) 4 kD dextran, (B) 40 kD dextran, and (C) 250 kDa dextran. Fluorescent images show a time lapse at 0, 90, and 240 s. Graphs show the averaged mean square displacement (MSD) curves over time. (D)

The molecular diffusion coefficients obtained for the different molecular weight dextran molecules is shown using two different analyses, MSD and fluorescent recovery after photobleaching (FRAP). (E) Summarized table of molecular diffusion coefficients found by MSD or FRAP, as well as the ratio of their experimentally-derived and theoretical values. Number of repetitions $n > 5$ for MSD and $n=4$ for FRAP. * Denotes a statistically significant difference where $p < 0.05$, ** $p < 0.01$, *** $p < 0.001$.
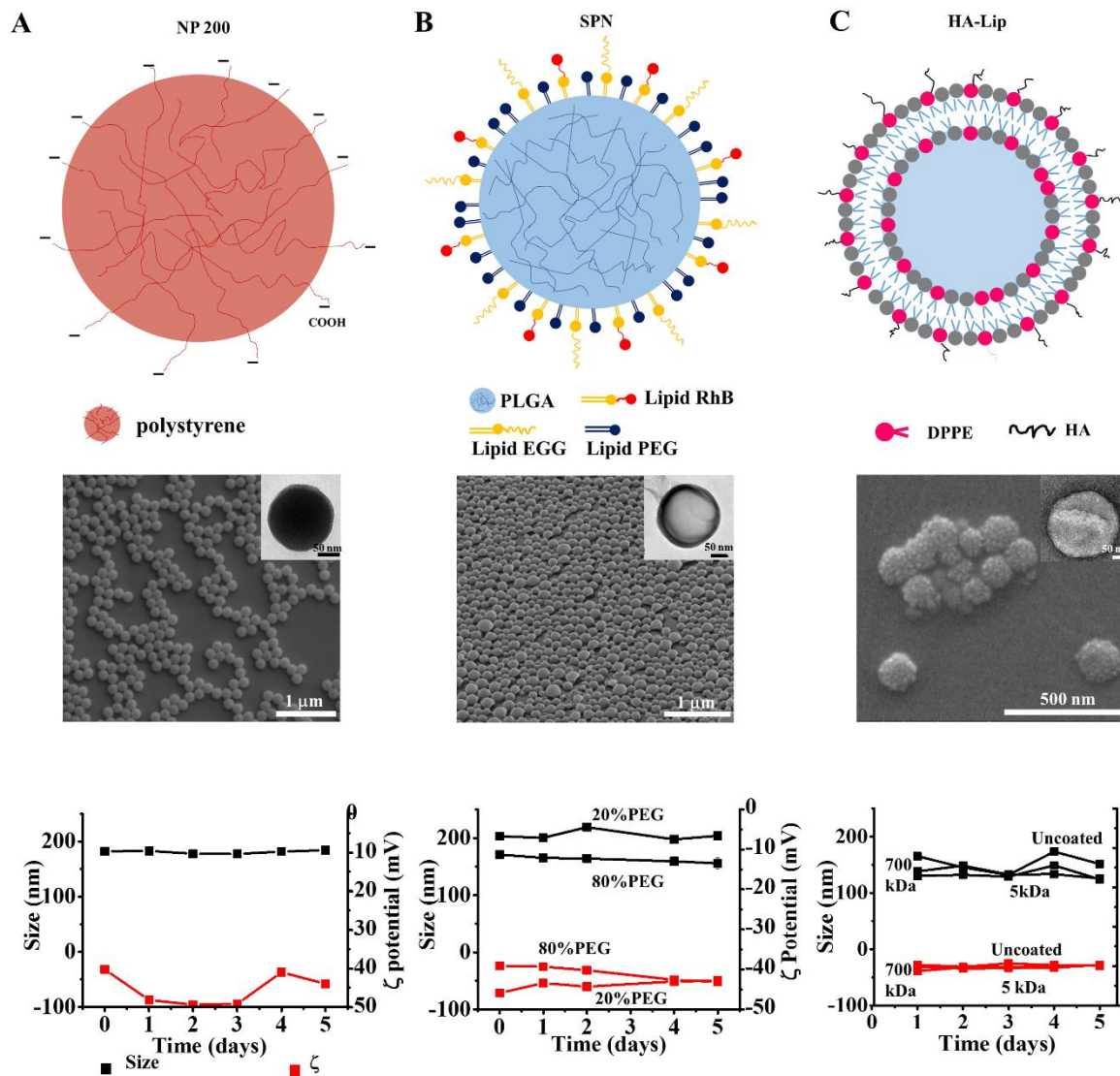
Figure 3. Schematic representations, electron microscopy images, dynamic light scattering (DLS) hydrodynamic size and ζ-potential measurements for (A) commercially available polystyrene carboxylate beads, (B) spherical PEGylated PLGA nanoparticles, and (C) liposomes coated with varying molecular weight hyaluronic acid. DLS and ζ-potential measurements were made over 5 days in water.
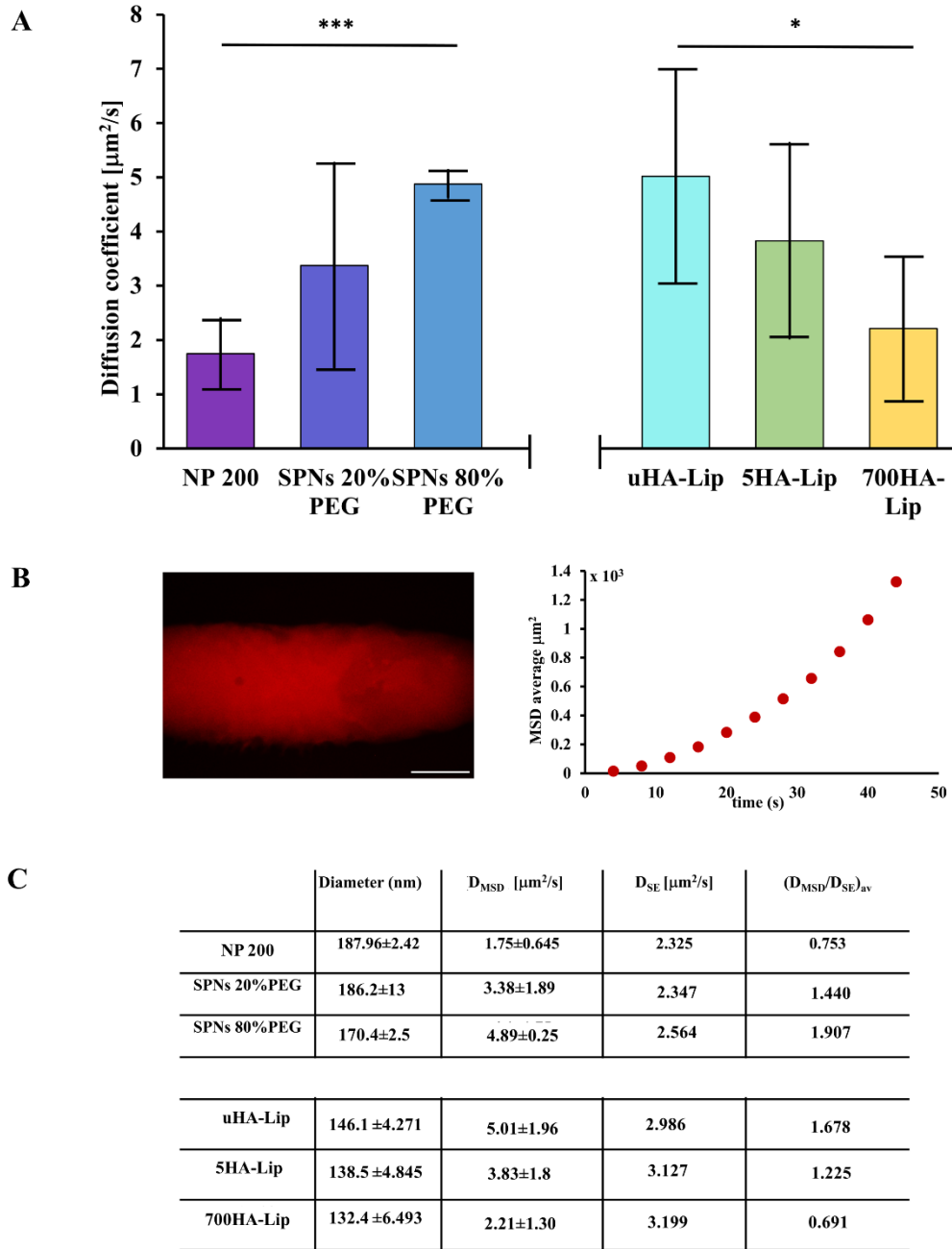
A

B

C

	Diameter (nm)	D_{MSD} [$\mu m^2/s$]	D_{SE} [$\mu m^2/s$]	$(D_{MSD}/D_{SE})_{av}$
NP 200	187.96±2.42	1.75±0.645	2.325	0.753
SPNs 20%PEG	186.2±13	3.38±1.89	2.347	1.440
SPNs 80%PEG	170.4±2.5	4.89±0.25	2.564	1.907
uHA-Lip	146.1±4.271	5.01±1.96	2.986	1.678
5HA-Lip	138.5±4.845	3.83±1.8	3.127	1.225
700HA-Lip	132.4±6.493	2.21±1.30	3.199	0.691

Figure 4. (A) Quantification of nanoparticles molecular diffusion coefficient was determined for nanoparticles using the MSD. (B) Representative fluorescent images of 5HA-Lip injected inside the Tissue Chamber and the corresponding the MSD plot. Scale bar represents 500 μm. (C) A table summarizing the nanoparticles diameters, and the MSD and Stokes-Einstein-derived molecular diffusion coefficients for the particles. N ≥ 4. * Denotes statistically significant difference $p < 0.05$, *** $p<0.001$.
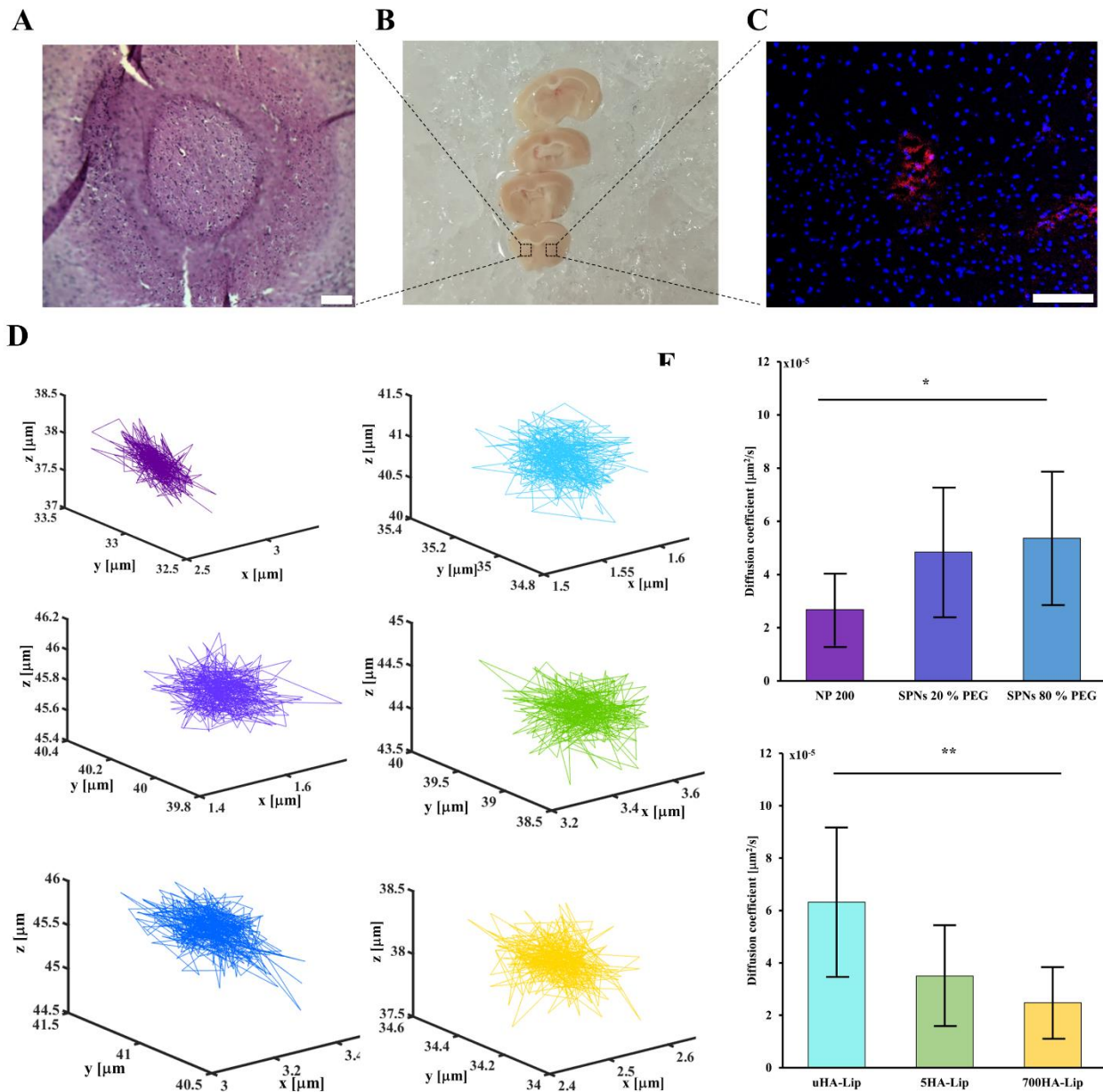
Figure 5. Ex-vivo single tracking and quantification of nanoparticles molecular diffusion coefficient. (A) Representative image of a 12 μm mouse brain slice stained with H&E with recognizable sign of the injection needle. Scale bar represents 100 μm. (B) Representative image of different brain sections. Squares highlight the striatum. (C) Confocal fluorescent microscopy image of a brain slice shows the NPs as red spots and the nuclei stained in DAPI. Scale bar represents 100 μm. (D) 3D trajectories of the particles diffusing through ex vivo brain slices. (E) Diffusion coefficients obtained for nanoparticles in the ex vivo brain tissue derived using MSD analysis. * Denotes a statistically significant difference p < 0.05, ** p < 0.01.
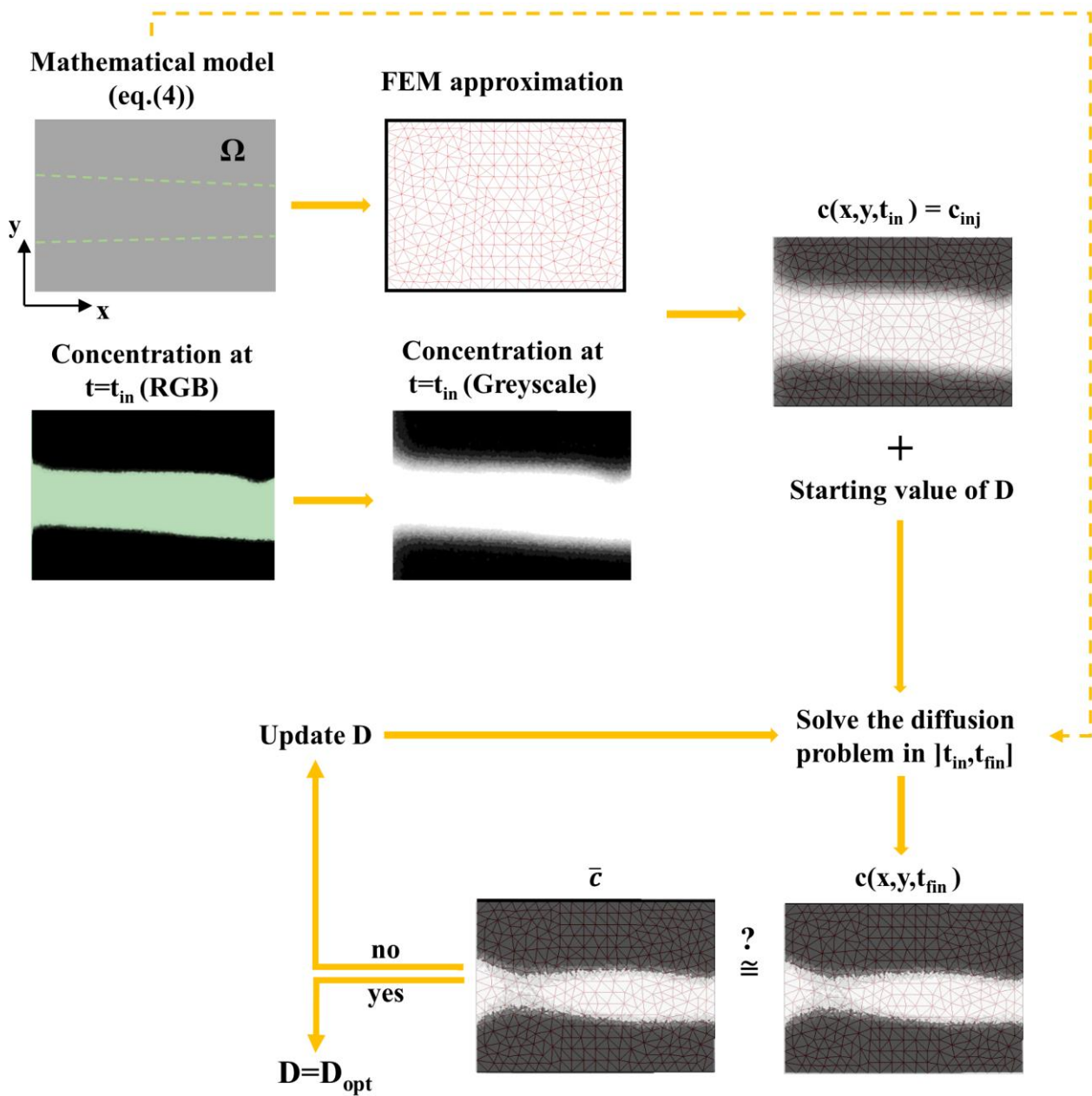
Figure 6. Quantification of the diffusion coefficient via an error minimization algorithm. Post-processing of the experimental data with conversion of the fluorescent microscopy images into greyscale maps and error minimization procedure implemented in the computational algorithm.

MOX Technical Reports, last issues

Dipartimento di Matematica
Politecnico di Milano, Via Bonardi 9 - 20133 Milano (Italy)

49/2019 Cicchetti, A.; Laurino, F.; Possenti, L.; Rancati, T.; Zunino, P.
In silico model of the early effects of radiation therapy on the microcirculation and the surrounding tissues

46/2019 Di Iorio, J.; Vantini, S.
funBI: a Biclustering Algorithm for Functional Data

47/2019 Spreafico, M.; Ieva, F.
Dynamic monitoring of the effects of adherence to medication on survival in Heart Failure patients: a joint modelling approach exploiting time-varying covariates

48/2019 Di Gregorio, S.; Fedele, M.; Pontone, G.; Corno, A.F.; Zunino, P.; Vergara, C.; Quarteroni, A.
A multiscale computational model of myocardial perfusion in the human heart

44/2019 Formaggia, L.; Gatti, F.; Zonca, S.
An XFEM/DG approach for fluid-structure interaction problems with contact

45/2019 Regazzoni, F.; Dedè, L.; Quarteroni, A.
Active force generation in cardiac muscle cells: mathematical modeling and numerical simulation of the actin-myosin interaction

43/2019 Antonietti, P.F.; Mazzieri, I.; Migliorini, F.
A space-time discontinuous Galerkin method for the elastic wave equation

41/2019 Abbà, A.; Bonaventura, L.; Recanati, A.; Tugnoli, M.;
Dynamical p-adaptivity for LES of compressible flows in a high order DG framework

42/2019 Martino, A.; Guatteri, G.; Paganoni, A.M.
hmmhdd Package: Hidden Markov Model for High Dimensional Data

39/2019 Lovato, I.; Pini, A.; Stamm, A.; Taquet, M.; Vantini, S.
Multiscale null hypothesis testing for network-valued data: analysis of brain networks of patients with autism